

A generating absorbing boundary condition for simulating wave interaction with maritime structures in current or at forward speed

Chang, X.; Wellens, P. R.

DOI

[10.1016/j.compfluid.2024.106216](https://doi.org/10.1016/j.compfluid.2024.106216)

Publication date

2024

Document Version

Final published version

Published in

Computers and Fluids

Citation (APA)

Chang, X., & Wellens, P. R. (2024). A generating absorbing boundary condition for simulating wave interaction with maritime structures in current or at forward speed. *Computers and Fluids*, 274, Article 106216. <https://doi.org/10.1016/j.compfluid.2024.106216>

Important note

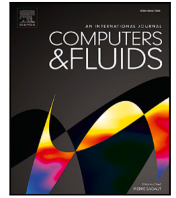
To cite this publication, please use the final published version (if applicable). Please check the document version above.

Copyright

Other than for strictly personal use, it is not permitted to download, forward or distribute the text or part of it, without the consent of the author(s) and/or copyright holder(s), unless the work is under an open content license such as Creative Commons.

Takedown policy

Please contact us and provide details if you believe this document breaches copyrights. We will remove access to the work immediately and investigate your claim.



A generating absorbing boundary condition for simulating wave interaction with maritime structures in current or at forward speed

X. Chang^a, P.R. Wellens^{b,*}

^a Shanghai Ship and Shipping Research Institute, Minsheng Rd. 600, Shanghai, 200135, China

^b Maritime and Transport Technology Department, Delft University of Technology, Mekelweg 2, Delft, 2628 CA, The Netherlands

ARTICLE INFO

Keywords:

Combined waves and mean flow
Absorbing boundary condition
Wave dispersion
Doppler shift
Volume of Fluid (VoF)

ABSTRACT

The lack of suitable boundary conditions in practical surface wave simulations with maritime structures in current or at forward speed may cause energy in the computational domain to accumulate due to spurious wave reflection. The common way to prevent wave reflection is to use passive wave absorbers, such as damping zones or relaxation zones, which requires larger domains at the cost of computational effort. Our goal is to derive a local generating absorbing boundary condition (GABC) for long-crested irregular waves on top of a mean flow, using the flow to model the forward speed of a structure such as a ship. Earlier work has demonstrated that a local GABC for free surface waves has a performance similar to passive wave absorbers, but at a reduced computational effort. New in the present work is that we extend, verify and validate the GABC in the presence of a nonzero mean flow. The GABC is designed to be accurate for a range of wave components in irregular sea states, with the resulting reflection coefficients for each component lower than a chosen value, say 5%. Having used potential flow theory for its derivation means that the boundary should not be placed at the exact location where wave breaking is expected, such as very close to the structure in the domain, or in the surf zone in coastal modeling. For the application with ships in this article that does not pose a limitation. The performance is demonstrated for a range of dimensionless wave number between 0 and 6. Such a boundary condition is obtained through a rational approximation of the linear dispersion relation with a mean flow, in combination with vertical derivatives of the solution variables along the boundary. Local linearization means that the GABC incorrectly considers bound, nonlinear wave components to be freely propagating wave components. Bound components, however, tend to have smaller amplitudes and do not appear to affect performance for the considered cases. Results of simulations with regular and irregular waves, on top of flows with different magnitudes and directions, are found to agree with the theory. The main source of differences is the implementation of the second derivative in the GABC near the free surface. Simulations of a Wigley hull at forward speed in irregular waves are compared to an experiment that was conducted specifically for validating the ABC. The data of the experiment are available as open data through doi: [10.4121/21320604](https://doi.org/10.4121/21320604). The comparison between simulation and experiment demonstrates that the GABC with a mean flow can be applied not only for theoretical simulations with propagating waves, but also for more practical applications with a structure in the domain.

1. Introduction

During the lifetime of ships and other maritime structures, they can be subject to harsh environmental conditions — wind, waves and currents. Currents can be wind-driven, be induced by wave breaking or originate from tides. They impose a mean load on structures. In heavy storms, time-varying wave loads add to the current loads. Waves and currents can also exert loads on the mooring system and thus induce vortex shedding. Modeling of waves at sea is incomplete without

currents and the combination of a mean flow and waves is an important aspect of simulating a realistic (nonlinear) loading conditions.

Computational Fluid Dynamics (CFD) – with the rapid development of high-performance computer hardware – has become more and more popular for engineers to evaluate the performance of wave structure interaction. However, numerical wave simulations become unrealistic if one does not make sure of preventing wave reflection from the boundaries of the computational domain. Reflected waves decrease the reliability of the solution field inside the domain by increasing

* Corresponding author.

E-mail address: p.r.wellens@tudelft.nl (P.R. Wellens).

<https://doi.org/10.1016/j.compfluid.2024.106216>

Received 13 October 2022; Received in revised form 31 December 2023; Accepted 15 February 2024

Available online 16 February 2024

0045-7930/© 2024 The Authors. Published by Elsevier Ltd. This is an open access article under the CC BY license (<http://creativecommons.org/licenses/by/4.0/>).

the energy level of the system, especially for longer simulations.

Passive wave absorption is a common approach to prevent wave reflection from domain boundaries. Various passive schemes have been thoroughly discussed in literature [1]. For example, the method of damping zones [2–4], also called sponge layers [5,6], includes momentum sources in the governing equation to dissipate the waves. Vertical velocity damping zones and pressure damping zones are more effective for shorter wave components than for longer wave components, because the dissipation is proportional to the vertical velocity. Vertical velocities in longer waves are small, and thus extra long zones are required to reduce reflection from a domain wall to a sufficient degree. Another approach is relaxation zones [7–11], which gradually force the computed wave field to comply with a theoretical field solution calculated with a far-field solver. Similarly to damping zones, relaxation zones perform well for short waves, but require longer zones to deal with long waves at the cost of computational efficiency [12,13].

In addition to passive wave absorption, there is also active wave absorption (AWA). AWA [14–16] relies on flow measurements, from which the incident and reflected wave signals can be separated with digital filters assuming the water is sufficiently shallow. This information (so-called feedback) is used to correct the wave generation boundary condition, in order to absorb the spurious waves while continuing to generate the target waves. The main advantage of this kind of AWA is that the domain does not need to be extended with zones, since AWA acts locally at the boundary itself. It has been developed from the shallow water assumption to the deep water conditions.

A third class is called absorbing boundary conditions (ABCs). ABCs can be categorized into two types: global and local ABCs. It has been discussed that global ABCs [17,18] are computationally undesirable, due to the requirement of storage of all previous time steps and processing of all grid points at each time step. ABCs, that are local in time and in space [19], can be as accurate as global ABCs in specific cases [20,21], but are more economical and straightforward to implement. Therefore, our strategy in this article is to derive a local ABC, continuing the work on those we did before [22,23].

Our ABCs are implemented in a method based on the Navier–Stokes equations, with a Volume-of-Fluid (VoF) approach for the free surface [24]. Before this study, one could use the method to either perform mean flow simulations, or to perform wave simulations, but not the combination. However, in reality waves and a mean flow, for instance induced by tides, are always present together. Absorbing boundary conditions (ABCs) for the combination of waves and a mean flow are a next step towards representing realistic environmental conditions. The objective of this study, therefore, is to derive a local ABC for long-crested irregular waves on top of a mean flow. Our main application is to use the mean flow to model the forward speed of a maritime structure such as a ship.

The article is structured as follows. After this brief introduction, the mathematical model is presented, including the governing equations and boundary conditions other than ABCs. Following that, a detailed discussion on the ABC accounting for both waves and flow is given. The stability of the ABC is discussed, after which it is verified against theoretical reflection coefficients, through a set of simulations of regular and irregular waves, on top of mean flows with different velocities and directions. Experiments of a Wigley hull at forward speed in head waves are performed to validate our ABC with mean flow. The main conclusions are repeated at the end of the article.

2. Mathematical model

Governing equations. A right-handed Cartesian system is employed and the axes are indicated by $\mathbf{x} = (x, y, z)$. The Navier–Stokes equations, derived from the conservation laws of mass and momentum, describe fluid flow in an arbitrary fixed control volume Ω with boundary Γ .

$$\int_{\Gamma} \mathbf{u} \cdot \mathbf{n} \, d\Gamma = 0 \quad (1)$$

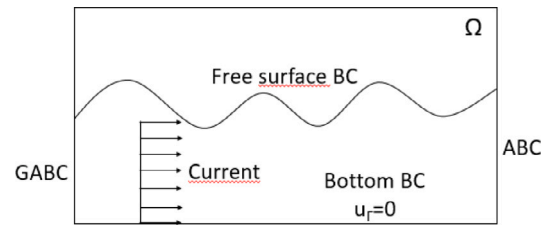


Fig. 1. Boundary conditions for the computational domain.

$$\int_{\Omega} \frac{\partial \mathbf{u}}{\partial t} \, d\Omega + \int_{\Gamma} \mathbf{u} \mathbf{u} \cdot \mathbf{n} \, d\Gamma + \frac{1}{\rho} \int_{\Gamma} p \mathbf{n} \, d\Gamma - \nu \int_{\Gamma} \mathbf{n} \cdot \nabla \mathbf{u} \, d\Gamma - \int_{\Omega} \mathbf{f} \, d\Omega = 0, \quad (2)$$

in which $\mathbf{u} = (u, v, w)$ represents the flow velocity in the axis direction, and \mathbf{n} denotes the outward normal vector to boundary Γ . ρ denotes the density of the fluid, p is the pressure and ν is the kinematic viscosity found from the ratio of dynamic viscosity μ over the density, $\nu = \mu/\rho$. Because of incompressibility, it is not required to solve a conservation law for energy in an additional equation. \mathbf{f} is a body force acting on the fluid, such as the force of gravity in the direction of the acceleration of gravity $(0, 0, -g)^T$.

In our application, the interface between water and air is of great interest, otherwise known as the free surface. As the flow is considered incompressible, the evolution of the free surface, $S(\mathbf{x}, t) = 0$, in space and time satisfies

$$\frac{\partial S}{\partial t} + \nabla \cdot (\mathbf{u}S) = 0. \quad (3)$$

Boundary conditions. Fig. 1 shows the computational domain with boundary conditions. In the simulations presented in this paper, the flow is often used to represent the forward speed of a ship so that boundary layers at domain walls are undesirable. Therefore, a free-slip condition has been adopted at the outer domain walls, as it allows for a coarser computational grid near the outer walls. Along the surface of the (moving) objects a no-slip condition $\mathbf{u} = \mathbf{u}_b$ has been chosen, where \mathbf{u}_b is the velocity of the object.

At the free surface, the normal and tangential forces are balanced leading to the boundary condition

$$\mu \left(\frac{\partial u_n}{\partial \tau} + \frac{\partial u_\tau}{\partial n} \right) = 0 \quad (4)$$

$$-p + 2\mu \frac{\partial u_n}{\partial n} = -p_0 + \sigma \kappa. \quad (5)$$

Here, subscripts n and τ denote the normal and tangential direction, respectively. The curvature of the free surface and surface tension are represented by κ and σ , respectively, while p_0 is the atmospheric pressure.

The boundary conditions for free surface waves applied at the inflow and outflow boundaries, left and right in Fig. 1 have been developed earlier and reported in Duz et al. [22] and Wellens and Borsboom [23]. They allow waves to propagate into and out of the computational domain simultaneously, and – for this reason – are called Absorbing Boundary Conditions (GABC). In this article, a (G)ABC is derived that accounts for the presence of a mean flow.

Potential flow. Our main application is the behavior of maritime structures in irregular free surface waves. Free surface waves near the boundary, which is sufficiently far from a structure in the path of wave propagation, can be assumed irrotational when not breaking and are well described by potential flow theory. The main limitation of the use of potential flow is that the boundary should not be placed at the exact location where waves can be expected to break during the length of the simulation. Examples of these locations are very close to a structure in the domain where waves are steeper due to diffracted and evanescent waves, and in the surf zone in coastal modeling. Potential

flow theory is used to impose the kinematics of free surface waves at the inflow boundary of the domain. Assuming irrotationality, a potential function ϕ is introduced, whose spatial derivative yields the velocity in the direction of the derivative. Superimposing undisturbed waves and mean flow, the following relation holds for the potential

$$\nabla\phi = \nabla(\phi_w + \mathbf{U} \odot \mathbf{x}) = \mathbf{u}_w + \mathbf{U} = \mathbf{u}, \tag{6}$$

in which ϕ_w and \mathbf{u}_w are the potential and velocity attributed to waves and \mathbf{U} is a mean uniform flow velocity in horizontal direction. Use of the potential leads to a reduced set of equations that in some instances can be solved analytically. With the potential the continuity equation becomes

$$\nabla^2\phi = 0. \tag{7}$$

After substitution of definition (6) into momentum Eq. (2) and integrating along a streamline, the momentum Eq. (2) becomes the unsteady Bernoulli equation

$$\frac{\partial\phi}{\partial t} + \frac{1}{2} |\nabla\phi|^2 + \frac{p}{\rho} - F = C, \tag{8}$$

in which F represents a body force and C is an integration constant.

3. Outflow boundary condition

Background. Damping zones or relaxation zones require a length of approximately two wave lengths to be effective. For short wave components, this comes at an acceptable cost, but for longer wave components damping zones and relaxation zones take up a significant part of the computational domain. While still possible in 2D domains for long-crested wave simulations, it can become infeasible in 3D because there may not be enough computer memory at one's disposal. For this reason this article focuses on local absorbing boundary condition that do not require increasing the domain size and come at hardly any additional computational cost. Alternative names for absorbing boundary conditions (ABCs) are non-reflecting boundary conditions or open boundary conditions.

Fourier transform of the planar wave equation can be used to derive a local ABC [25]. This procedure has also been summarized in [18]. A first-order approximation of the dispersion relation obtained after transformation yields a first-order ABC, also known as a Sommerfeld condition, and higher-order approximations give higher derivatives in the ABC with which waves propagating in different directions are accurately absorbed [26].

To account for the dispersive property of waves, i.e. waves at different frequencies propagate at different phase velocities, a higher-order ABC is one of the approaches, because it contains a number of coefficients that together span a range of phase velocities for which the ABC gives little reflection. Alternatively, a low-order boundary condition in combination with an estimate of the instantaneous phase velocity at the boundary has been proposed by [27]. This estimate can lead to division-by-zero instabilities and therefore this approach should not be adopted.

ABCs have also been investigated from the point of view of characteristic variables [28–30]. This approach diagonalizes the system of equations at hand to identify characteristic lines along which information propagates into the domain or out. The part of the equations after diagonalization that lets wave information propagate out is used as a boundary condition.

Other researchers derive ABCs by factoring the wave equation into components which represent the incoming and outgoing waves. The components that prescribe the incoming wave field are then used to design the absorbing boundary condition. Factorization has been used to derive ABCs for the 2-D acoustic equation [31] and for the acoustic and elastic wave equations [25]. These results are later extended to the one-way wave equation for migration [32]. This strategy has also been adopted in our own work on ABCs and generating absorbing boundary

conditions (GABCs), see Duz et al. [22] and Wellens and Borsboom [23].

The wave equation is decomposed in a somewhat different way from factorization in [33]. It leads to local absorbing boundary conditions obtained directly from the outgoing components of the wave field. It is not necessary to approximate the outgoing components of the wave field, as is the case with factorization of the wave equation. As the derivation of the ABC in this article follows this approach and adapts it for use with a range of phase velocities (dispersion), it is discussed next.

Decomposition of the wave equation. The planar wave equation is decomposed into the individual components representing incoming and outgoing waves respectively. The outgoing wave component is adopted to design an absorbing boundary condition [33].

Decomposition into wave components implies linearization, potentially affecting performance in nonlinear wave simulations. The linearization is local in space and limited to the position of the boundary of the domain. The nonlinear transfer of energy between components and the formation of bound components requires space and it therefore only marginally affected by a local linearization near the boundary. The boundary condition also does not affect the nonlinear processes that take place inside the computational domain.

We will study waves with a two-dimensional wave number vector $\mathbf{k} = (k_x, k_y)$, whose length is denoted by $k \equiv |\mathbf{k}| = \sqrt{k_x^2 + k_y^2}$. The wave number components k_x and k_y can be complex valued to distinguish between propagating and evanescent/spurious waves (see [23] for the latter). The unit vector in the wave direction \mathbf{k} is represented by \mathbf{e}_k .

With the unit vector \mathbf{e}_k , the planar wave equation can be decomposed as follows

$$\nabla^2\phi - \frac{1}{c^2} \frac{\partial^2\phi}{\partial t^2} = \left(\nabla + \frac{\mathbf{e}_k}{c} \frac{\partial}{\partial t}\right) \left(\nabla - \frac{\mathbf{e}_k}{c} \frac{\partial}{\partial t}\right) \phi = 0. \tag{9}$$

A plane wave propagating in the direction \mathbf{e}_k with velocity c has the form $\phi = \phi(\mathbf{x} \cdot \mathbf{e}_k - ct)$. Applying the first factor in Eq. (9) to the plane wave $\phi = \phi(\mathbf{x} \cdot \mathbf{e}_k - ct)$ results in

$$\left(\nabla + \frac{\mathbf{e}_k}{c} \frac{\partial}{\partial t}\right) \phi = 0. \tag{10}$$

This means that the factor $\nabla + (\mathbf{e}_k/c)(\partial/\partial t)$ can be used to identify plane waves traveling in the direction \mathbf{e}_k . Similarly, the second factor in Eq. (9) corresponds to those waves propagating in the opposite direction $-\mathbf{e}_k$. If outgoing waves are propagating in the direction \mathbf{e}_k , the operator $\nabla + (\mathbf{e}_k/c)(\partial/\partial t)$ can be used to design a boundary condition which absorbs these waves without reflection.

In the original boundary condition [33], the wave propagation direction \mathbf{e}_k was used as a main parameter to absorb plane waves propagating in different directions. In this article, incoming waves are unidirectional so that \mathbf{e}_k is fixed along the entire domain boundary. Our work focuses on how to account for the effect of wave dispersion in the presence of a mean flow.

Dispersion relation for linear waves and uniform mean flow. Consider a body of water with a uniform depth and a free surface denoted η_w . Considering potential flow and a uniform mean flow \mathbf{U} , the linear kinematic and dynamic boundary conditions at the free surface are

$$\begin{aligned} \frac{\partial\eta_w}{\partial t} + \left(U_x + \frac{\partial\phi_w}{\partial x}\right) \frac{\partial\eta_w}{\partial x} + \left(U_y + \frac{\partial\phi}{\partial y}\right) \frac{\partial\eta_w}{\partial y} - \frac{\partial\phi_w}{\partial z} &= 0 \Big|_{z=\eta}, \\ g\eta_w + \frac{\partial\phi_w}{\partial t} + \frac{1}{2} |\nabla\phi_w + \mathbf{U}|^2 &= C \Big|_{z=\eta}. \end{aligned} \tag{11}$$

where U_x and U_y are the components of the uniform mean flow \mathbf{U} . The subscript w denotes the contribution only from waves. By choosing constant $C = \frac{1}{2}U^2$ and ignoring the second-order terms, we obtain the following relations

$$\frac{\partial\eta_w}{\partial t} + \mathbf{U} \cdot \nabla\eta_w = \frac{\partial\phi_w}{\partial z} \Big|_{z=\eta}, \tag{12}$$

$$\frac{\partial \phi_w}{\partial t} + \mathbf{U} \cdot \nabla \phi_w + g \eta_w = 0 \Big|_{z=\eta} \quad (13)$$

Using the latter, which is a linearized Bernoulli equation, to eliminate the surface displacement η_w from the kinematic condition (12) gives (after multiplication with g)

$$\left(\frac{\partial}{\partial t} + \mathbf{U} \cdot \nabla \right)^2 \phi_w = -g \frac{\partial \phi_w}{\partial z} \Big|_{z=\eta} \quad (14)$$

For small amplitude waves, the relation at the exact position $z = \eta$ are approximately satisfied at the mean free surface $z = 0$. Waves of the form $\phi_w = \phi_a e^{i(\mathbf{k} \cdot \mathbf{x} - \omega t)} \cosh(|\mathbf{k}|z)$ with amplitude ϕ_a satisfy the linearized boundary conditions and the continuity equation. Using this form, (14) becomes

$$g \frac{\partial \phi_w}{\partial z} \Big|_{z=0} = -c_{k0}^2 \nabla \cdot \nabla \phi_w \Big|_{z=0}, \quad c_{k0}^2 \equiv g (\tanh |\mathbf{k}|h) / |\mathbf{k}| \quad (15)$$

The notation c_{k0} is the propagation speed without flow (hence the 0). Substitution of the relation (14) into Eq. (15) gives

$$\left(\frac{\partial}{\partial t} + \mathbf{U} \cdot \nabla \right)^2 \phi_w = c_{k0}^2 \nabla \cdot \nabla \phi_w \quad (16)$$

Working out the derivatives together with the expression for ϕ_w leads to the dispersion relation in the presence of a mean flow

$$\omega_{\pm} - \mathbf{U} \cdot \mathbf{k} = \pm c_{k0} |\mathbf{k}| \quad (17)$$

Using the linear dispersion relation potentially affects the performance of the boundary condition in nonlinear wave simulations. That effect will be strongest for regular wave simulations. For steep, regular waves there is a difference between the nonlinear phase velocity and the linear phase velocity. That difference will make the reflection coefficient of the boundary condition larger. The wave components of higher order than first order also bound to the base component, whereas the boundary condition will consider them as free wave components with their own phase velocity. In nonlinear, irregular wave simulations the amplitudes of higher-order wave components are much smaller than for steep regular waves. The difference in phase velocity for the many wave components in the decomposition is also smaller in irregular waves than in regular waves. Therefore, in irregular wave simulations the limitation of using linearized theory locally, only at the position of the boundary, is not thought to affect the performance of the boundary condition substantially.

Solution of the dispersion relation for linear waves and uniform mean flow.

For a given frequency ω , the solution of dispersion relation (17) will depend on the angle between the wave direction and the direction of the mean flow. The right-hand side of (17), $c_{k0} |\mathbf{k}|$, will be referred as $\sigma(k)$. For the situation that \mathbf{k} is real and the wave direction and mean flow direction are the parallel, Fig. 2, reproduced from [34,35], indicates the solutions of the dispersion relation. The dashed line parallel to the k -axis in Fig. 2 represents the solution for the situation without mean flow. One solution, indicated as point E, then exists. The other solutions, indicated as points A to D with wave numbers k for which $\sigma(k)$ is equal to $\omega - \mathbf{U} \cdot \mathbf{k}$. Solutions A and B are for an opposing mean flow, solutions C and D are for a following mean flow.

In maritime applications, solutions A and C are the ones of most interest. Compared to the situation without flow, a following mean flow increases the wave length and an opposing mean flow decreases the wave length. Solutions B and D, which do not exist if there is no mean flow, correspond to shorter waves than A and C. Solution B corresponds to waves propagating against the flow, but with energy transport $\partial \sigma(k) / \partial k$ in the direction of the flow. Solution D corresponds to waves propagating in the direction of the flow, but with wave energy in opposite direction to the flow. For a sufficiently large flow velocity in opposite direction to the wave direction, solutions A and B do not exist, meaning that propagating wave modes do not exist under these circumstances.

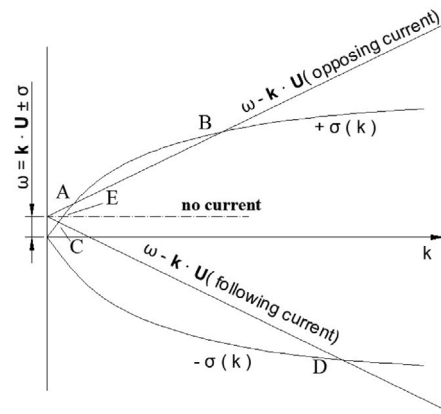


Fig. 2. Solution of the dispersion relation for linear waves on top of uniform mean flow. The figure is from the work of [35].

4. Derivation of the ABC with a mean flow

Rewriting boundary condition (10) using the parameters from the dispersion relation gives

$$\left(|\mathbf{k}| \mathbf{e}_k \frac{\partial}{\partial t} + \omega \nabla \right) \phi_w = 0 \quad (18)$$

Eq. (18) is a boundary condition with zero reflection for waves of the form $\phi_w = \phi_a e^{i(\mathbf{k} \cdot \mathbf{x} - \omega t)} \cosh(|\mathbf{k}|z)$. Substitution of the dispersion relation (17) into (18) and division by $|\mathbf{k}|$ leads to

$$\left(\mathbf{e}_k \frac{\partial}{\partial t} + (U + c_{k0}) \nabla \right) \phi_w = 0 \quad (19)$$

which is a vector relation. Here $U = \mathbf{U} \cdot \mathbf{k}$. Dot-multiplying it with a vector \mathbf{n} in normal direction to the boundary results in

$$\left(\mathbf{n} \cdot \mathbf{e}_k \frac{\partial}{\partial t} + (U + c_{k0}) \frac{\partial}{\partial n} \right) \phi_w = 0 \quad (20)$$

Boundary condition (20) is the basis of the further derivations. It is of the Sommerfeld type with zero reflection of a single wave component with frequency ω propagating in direction \mathbf{e}_k on top of a mean flow U . The reflection is larger for wave components with other frequencies and directions [23].

Approximation of the dispersion relation. For simulations with irregular waves, with multiple wave components at the same time, we would like the boundary condition (20) to have little reflection not for a single wave component, but for a range of wave components. Following [23], the first step of two steps in obtaining a boundary condition for a range of wave components is to approximate the dispersion relation. The better we approximate the dispersion relation, the less reflection we obtain. A rational polynomial in kh is introduced, where $k = |\mathbf{k}| = \sqrt{k_x^2 + k_y^2}$, to approximate the dispersion relation [23]:

$$c_{k0} = \sqrt{gh} \sqrt{\frac{\tanh(kh)}{kh}} \approx \sqrt{gh} \frac{a_0 + a_1(kh)^2}{1 + b_1(kh)^2} \quad (21)$$

The coefficients a_0 , a_1 and b_1 can be chosen such that for different application, different kh -ranges of the dispersion relation are approximated well.

The second step in obtaining a boundary condition for a range of wave components is to replace wave number k with an operation on the solution variables. For waves of the form $\phi_w = \phi_a e^{i(\mathbf{k} \cdot \mathbf{x} - \omega t)} \cosh(|\mathbf{k}|z)$, taking the second derivative of the solution variable in z -direction yields k^2 times that same solution variable

$$\frac{\partial^2 \phi_w}{\partial z^2} = k^2 \phi_w \quad (22)$$

ABC with a mean flow. Considering waves of the form $\phi_w = \phi_a e^{i(\mathbf{k}\cdot\mathbf{x} - \omega t)} \cosh(|\mathbf{k}z|)$. Substitution of the approximate dispersion relation (21) and relation (22) into boundary condition (20) leads to an absorbing boundary condition (ABC) in the presence of a mean flow

$$\begin{aligned} & (\mathbf{n} \cdot \mathbf{e}_k) \left(\frac{\partial \phi_w}{\partial t} + b_1 h^2 \frac{\partial(\partial^2 \phi_w / \partial z^2)}{\partial t} \right) \\ & + \left(\frac{\partial \phi_w}{\partial n} + b_1 h^2 \frac{\partial(\partial^2 \phi_w / \partial z^2)}{\partial n} \right) U_k \\ & + \left(\sqrt{gh} a_0 \frac{\partial \phi_w}{\partial n} + a_1 h^2 \frac{\partial(\partial^2 \phi_w / \partial z^2)}{\partial n} \right) \\ & = (\mathbf{n} \cdot \mathbf{e}_k) \left(\frac{\partial \phi_w}{\partial t} + b_1 h^2 \partial^2 / \partial z^2 \frac{\partial \phi_w}{\partial t} \right) \\ & + \left(\frac{\partial \phi_w}{\partial n} + b_1 h^2 \partial^2 / \partial z^2 \frac{\partial \phi_w}{\partial n} \right) U_k \\ & + \left(\sqrt{gh} a_0 \frac{\partial \phi_w}{\partial n} + a_1 h^2 \partial^2 / \partial z^2 \frac{\partial \phi_w}{\partial n} \right) \\ & = \left[(\mathbf{n} \cdot \mathbf{e}_k) \left(1 + b_1 h^2 \frac{\partial^2}{\partial z^2} \right) \frac{\partial}{\partial t} + \right. \\ & \left. \left(\left(1 + b_1 h^2 \frac{\partial^2}{\partial z^2} \right) U_k + \sqrt{gh} \left(a_0 + a_1 h^2 \frac{\partial^2}{\partial z^2} \right) \right) \frac{\partial}{\partial n} \right] \phi_w = 0. \end{aligned} \quad (23)$$

GABC with a mean flow. At the inflow boundary, incoming waves need to be specified while preventing re-reflection of outgoing waves simultaneously. Following [23], non-zero right-hand side consisting of the same combination of operators applied to the incoming wave potential is prescribed leading to a generating and absorbing boundary condition (GABC) in the presence of a mean flow

$$\begin{aligned} & \left[(\mathbf{n} \cdot \mathbf{e}_k) \frac{\partial}{\partial t} + \left(U_k + \sqrt{gh} \frac{a_0 + a_1 h^2 \partial^2 / \partial z^2}{1 + b_1 h^2 \partial^2 / \partial z^2} \right) \frac{\partial}{\partial n} \right] \phi_w \\ & = \left[(\mathbf{n} \cdot \mathbf{e}_k) \frac{\partial}{\partial t} + \left(U_k + \sqrt{gh} \frac{a_0 + a_1 h^2 \partial^2 / \partial z^2}{1 + b_1 h^2 \partial^2 / \partial z^2} \right) \frac{\partial}{\partial n} \right] \phi_{in}. \end{aligned} \quad (24)$$

Here ϕ_{in} denotes the incoming wave potential that is of the form ϕ_w used earlier.

ABC in terms of primitive variables. The ABC in Eq. (23) and GABC in (24) with a mean flow are utilized as boundary conditions for outgoing waves in a method, based on [24], that solves for velocities and pressures. The solution variables are staggered within a cell. The domain boundary is chosen such that it coincides with the position of the horizontal velocity u_b . It is essential that the velocity and pressure in this boundary condition are defined at the same position. Any other configuration would lead to phase differences between solution variables at the boundary and additional spurious reflection.

In potential theory, the velocity in n -direction is defined to be the derivative of the potential in that direction

$$\frac{\partial \phi_w}{\partial n} = \mathbf{u}_w \cdot \mathbf{n} = (\mathbf{u}_b - \mathbf{U}) \cdot \mathbf{n}. \quad (25)$$

The subscript w describes the velocity only due to waves. The subscript b here indicates the total velocity, defined exactly on the domain boundary, attributed to both waves and the mean flow. To obtain the expression for the pressure, the linearized Bernoulli equation is used

$$\frac{\partial \phi_w}{\partial t} = -\frac{p_b}{\rho} - gz - \mathbf{u}_w \cdot \mathbf{U}. \quad (26)$$

Again the subscript b implies that the pressure is specified at the domain boundary and obtained from linear interpolation of the pressures in the cells on either side of the boundary. Substitution of relations (25) and (26) into (23) yields

$$\begin{aligned} & (\mathbf{n} \cdot \mathbf{e}_k) \left(1 + b_1 h^2 \frac{\partial^2}{\partial z^2} \right) \left(-gz - \frac{p_b}{\rho} - \mathbf{u}_w \cdot \mathbf{U} \right) \\ & + \left[U_k \left(1 + b_1 h^2 \frac{\partial^2}{\partial z^2} \right) + \sqrt{gh} \left(a_0 + a_1 h^2 \frac{\partial^2}{\partial z^2} \right) \right] (\mathbf{u}_w \cdot \mathbf{n}) = 0. \end{aligned} \quad (27)$$

Since the following relation holds

$$\begin{aligned} U_k \mathbf{u}_w \cdot \mathbf{n} & = (\mathbf{U} \cdot \mathbf{e}_k)(\mathbf{n} \cdot \nabla) \phi_w = (\mathbf{U} \cdot \mathbf{e}_k)(\mathbf{n} \cdot \mathbf{k}) \phi'_w \\ & = (\mathbf{n} \cdot \mathbf{e}_k)(\mathbf{U} \cdot \mathbf{k}) \phi'_w = (\mathbf{n} \cdot \mathbf{e}_k)(\mathbf{U} \cdot \nabla) \phi_w \\ & = (\mathbf{n} \cdot \mathbf{e}_k)(\mathbf{u}_w \cdot \mathbf{U}), \end{aligned} \quad (28)$$

in which ϕ'_w is the derivative of ϕ_w in the direction of \mathbf{k} , the (G)ABC with a mean flow (27) is written as follows

$$\begin{aligned} & (\mathbf{n} \cdot \mathbf{e}_k) \left(1 + b_1 h^2 \frac{\partial^2}{\partial z^2} \right) \left(-gz - \frac{p_b}{\rho} \right) \\ & + \sqrt{gh} \left(a_0 + a_1 h^2 \frac{\partial^2}{\partial z^2} \right) [(\mathbf{u}_b - \mathbf{U}) \cdot \mathbf{n}] = 0. \end{aligned} \quad (29)$$

This is the form that is implemented in the method used for evaluating the performance of the (G)ABC below.

5. Stability analysis

A Sommerfeld type boundary condition has zero reflection for a single wave component with frequency ω and a much larger reflection for wave components with other frequencies. (G)ABC (29) has a large range of wave components it can absorb, at the expense of some reflection, say less than 5%, for all wave components in that range. The reflection coefficient for the (G)ABC in the presence of a mean flow is derived in Appendix. In addition to reflected wave components, it was found in [23] that spurious wave components that grow in time could exist, leading to instability if the coefficients a_0, a_1 and b_1 in approximation (21) did not satisfy specific criteria. The criteria were found by studying the reflection coefficient (ratio of reflected wave amplitude over incoming wave amplitude) at the boundary, for the different types of wave components that the system of equations allows for. The system of equations allows for propagating wave modes, evanescent wave modes and the spurious wave modes. In the situation without a mean flow, propagating wave modes generate reflected wave modes with the same frequency and a similar vertical velocity profile. Evanescent wave modes are not created by the (G)ABC, but if present due to an object nearby (a modeled maritime structure), then their reflection coefficient is 1. Spurious wave modes do not exist if the coefficients satisfy the criteria.

In the situation with a mean flow, the reflected wave components have a different wave length due to the Doppler effect. Due to the wave number being different, they also have a different vertical velocity profile. Because of the differences in the vertical velocity profile between incoming wave modes and reflected wave modes, the (G)ABC can generate evanescent wave modes. The reflection coefficient of evanescent wave modes does not change in the present of a mean flow, and remains equal to 1 for all wave frequencies. And if the reflection coefficient is small, the amplitudes of the evanescent wave modes will be small. Spurious wave components are also still not generated if the coefficients in the approximation satisfy specific criteria. Those criteria are the same as for the situation without mean flow and repeated here from [23] to be complete

$$\frac{a_0}{\pi^2} < a_1 < \frac{4a_0}{\pi^2} \quad \text{and} \quad a_1 < b_1 < \frac{4}{\pi^2}. \quad (30)$$

The stability of the boundary condition when using these coefficients is demonstrated below by means of a long duration simulation.

6. Numerical implementation

The (G)ABC in Eq. (29) is discretized and incorporated in a numerical method. The method employs a finite volume method (FVM) on a fixed Cartesian grid with a staggered arrangement of variables for the discretization of the governing equations. The structural geometry is described by means of the cut-cell approach. The free surface is transported by means of a Volume-of-Fluid (VoF) method.

Using the notation in [23,24], the discrete system of equations becomes

$$\mathcal{M}\mathbf{u}_h^{n+1} = 0. \quad (31)$$

$$\mathcal{V} \frac{\mathbf{u}_h^{n+1} - \mathbf{u}_h^n}{\Delta t} = -C(\mathbf{u}_h^n)\mathbf{u}_h^n + \nu D\mathbf{u}_h^n - \frac{1}{\rho} \mathcal{G}\mathbf{p}_h^{n+1} + \mathbf{f}_h^n. \quad (32)$$

Here, \mathcal{M} is a divergence matrix for the discrete continuity equation, \mathcal{V} a diagonal matrix containing the control volume size, $C(\mathbf{u}_h^n)$ a convective operator, D a diffusion operator and \mathcal{G} a gradient operator. The vector \mathbf{u}_h contains the discrete velocities, \mathbf{p}_h contains the discrete pressure and \mathbf{f}_h accounts for the discrete gravity. For the purpose of energy preservation, the pressure should not contribute to the energy balance. Therefore, the discrete pressure gradient \mathcal{G} needs to be related to the discrete divergence operator as $\mathcal{G} = -\mathcal{M}^T$.

An auxiliary vector $\tilde{\mathbf{u}}_h$, containing the contributions of convection, diffusion and gravity at the old time level, is introduced

$$\tilde{\mathbf{u}}_h^n = \mathbf{u}_h^n - (C(\mathbf{u}_h^n)\mathbf{u}_h^n - \nu D\mathbf{u}_h^n - \mathbf{f}_h^n). \quad (33)$$

With the auxiliary velocity $\tilde{\mathbf{u}}_h$, the discrete momentum Eq. (32) becomes

$$\mathbf{u}_h^{n+1} = \tilde{\mathbf{u}}_h^n - \Delta t \mathcal{V}^{-1} \frac{1}{\rho} \mathcal{M}^T \mathbf{p}_h^{n+1}. \quad (34)$$

Substitution of the momentum equation into the continuity equation and rearranging terms result in a discrete Poisson equation for the pressure

$$\mathcal{M}\mathcal{V}^{-1}\mathcal{M}^T \mathbf{p}_h^{n+1} = \frac{\rho}{\Delta t} \mathcal{M}\tilde{\mathbf{u}}_h^n. \quad (35)$$

The pressure at the new time level p_h^{n+1} in the above equation can be solved with a linear solver. A Bi-CGSTAB solver with an incomplete LU preconditioner has been adopted. The solution p_h^{n+1} in system (35) is used to calculate the velocities \mathbf{u}_h^{n+1} from Eq. (34).

A (G)ABC contains a combination of pressure and velocity and we want to apply it at the inflow and outflow boundaries of the domain. At the boundary, the velocity is defined, but the pressure is defined half a mesh size away because of staggering the variables.

We choose $\mathbf{n} = \mathbf{e}_x$ in the equation and present the boundary conditions for this situation. Adding the spatial and temporal level to the variables p_b and \mathbf{u}_b in the boundary condition (29) yields

$$\begin{aligned} & (\mathbf{e}_x \cdot \mathbf{e}_k) \left(1 + b_1 h^2 \frac{\partial^2}{\partial z^2} \right) \left(-gz - \frac{p_{b,k}^{n+1}}{\rho} \right) \\ & + \sqrt{gh} \left(a_0 + a_1 h^2 \frac{\partial^2}{\partial z^2} \right) [(\mathbf{u}_{b,k}^{n+1} - \mathbf{U}) \cdot \mathbf{e}_x] = 0. \end{aligned} \quad (36)$$

The pressure at the boundary $p_{b,k}^{n+1}$ is obtained from linear interpolation between the pressures in cells on either side of the boundary

$$p_{b,k}^{n+1} = \frac{1}{2}(p_{i,k} + p_{i+1,k})^{n+1}, \quad (37)$$

in which the locations of the pressures near the boundary $p_{b,k}$, $p_{i,k}$ and $p_{i+1,k}$ are shown in Fig. 3.

It is essential that the velocity and the pressure at the boundary are defined at the same point in time. The pressures and velocities at the boundary are determined at time t^{n+1} . We will discuss the discretization of the (G)ABC in the xz -plane. Therefore, the x -component of the term $(\mathbf{u}_{b,k}^{n+1} - \mathbf{U}) \cdot \mathbf{n}$ is written as $u_{b,k}^{n+1} - U_x$.

The horizontal velocity at the new time level $u_{b,k}^{n+1}$ can be eliminated by means of the momentum equation at the boundary

$$u_{b,k}^{n+1} = u_{i,k}^{n+1} = \tilde{u}_{i,k} - \frac{1}{\rho} \frac{\Delta t}{\Delta x_{i+1,k}} (p_{i+1,k} - p_{i,k})^{n+1}. \quad (38)$$

Note that \tilde{u} contains convective and diffusive terms. Substituting the expressions (37) through (38) into Eq. (36) yields

$$(\mathbf{e}_x \cdot \mathbf{e}_k) \left(1 + b_1 h^2 \frac{\partial^2}{\partial z^2} \right) \left(-gz - \frac{1}{2}(p_{i,k} + p_{i+1,k})^{n+1} \right)$$

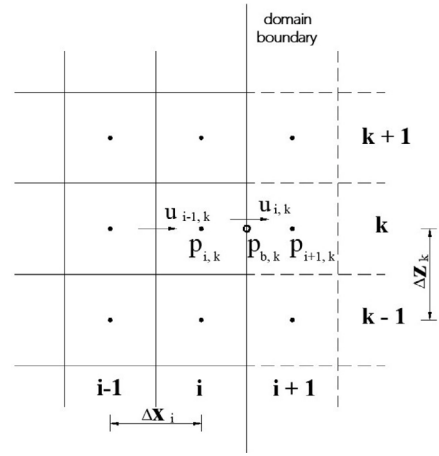


Fig. 3. Pressure at the domain boundary is calculated from the linear interpolation of the pressure on either side of the boundary.

$$\begin{aligned} & + \sqrt{gh} \left(a_0 + a_1 h^2 \frac{\partial^2}{\partial z^2} \right) \cdot \\ & \left(\tilde{u}_{i,k} - \frac{1}{\rho} \frac{\Delta t}{\Delta x_{i+1,k}} (p_{i+1,k} - p_{i,k})^{n+1} - U_x \right) = 0. \end{aligned} \quad (39)$$

For the approximation of the second derivation in z -direction, the following operator \mathcal{Q} , designed for a stretched grid, is employed

$$\mathcal{Q} = \begin{bmatrix} \mathcal{Q}_1 \\ \mathcal{Q}_2 \\ \mathcal{Q}_3 \end{bmatrix} = \frac{1}{\frac{1}{2} \Delta z_{i,k} \Delta z_{i,k+1} (\Delta z_{i,k} + \Delta z_{i,k+1})} \begin{bmatrix} \Delta z_{i,k} \\ -\Delta z_{i,k} - \Delta z_{i,k+1} \\ \Delta z_{i,k+1} \end{bmatrix}. \quad (40)$$

Here $\Delta z_{i,k} = z_{i,k} - z_{i,k-1}$ and $\Delta z_{i,k+1} = z_{i,k+1} - z_{i,k}$, with $z_{i,k-1}$, $z_{i,k}$ and $z_{i,k+1}$ being the center locations of the pressure variables $p_{i,k-1}$, $p_{i,k}$ and $p_{i,k+1}$ in Fig. 3. The operator \mathcal{Q} operates on the vectors \mathbf{p} and $\tilde{\mathbf{u}}$.

Now the following notations are introduced

$$\begin{aligned} \varphi &= \sqrt{gh} a_0, \quad \chi = \sqrt{gh} a_1 h^2, \\ \psi &= (\mathbf{e}_x \cdot \mathbf{e}_k) b_1 h^2, \quad \tau = \frac{1}{\rho} \frac{\Delta t}{\Delta x}, \\ \mathbf{p}_i &= \begin{bmatrix} p_{i,k-1} \\ p_{i,k} \\ p_{i,k+1} \end{bmatrix}, \quad \mathbf{u}_i = \begin{bmatrix} \tilde{u}_{i,k-1} \\ \tilde{u}_{i,k} \\ \tilde{u}_{i,k+1} \end{bmatrix}. \end{aligned} \quad (41)$$

The terms of unknown variables are arranged to be on the left-hand side, and the terms with known variables on the right-hand side. The second derivatives in z -direction of the variables gz and U_x , i.e. $\frac{\partial^2}{\partial z^2}(gz)$ and $\frac{\partial^2}{\partial z^2} U_x$, are zero. Applying the operator in (40) and the notations in (41) to Eq. (39), a discrete equation for the (G)ABC is obtained

$$\begin{aligned} & [B_{zl} \ B_c \ B_{zr}] \mathbf{p}_i + [B_{rl} \ B_{rc} \ B_{rr}] \mathbf{p}_{i+1} \\ & = [\mathcal{E}_{zl} \ \mathcal{E}_c \ \mathcal{E}_{zr}] \tilde{\mathbf{u}}_i + (\mathbf{n} \cdot \mathbf{e}_k) gz + \varphi U_x, \end{aligned} \quad (42)$$

with the coefficients

$$\begin{aligned} B_{zl} &= (-\chi \tau + \frac{1}{2} \psi) \mathcal{Q}_1, \\ B_c &= -\varphi \tau + \frac{1}{2} (\mathbf{n} \cdot \mathbf{e}_k) - (\chi \tau - \frac{1}{2} \psi) \mathcal{Q}_2, \\ B_{zr} &= (-\chi \tau + \frac{1}{2} \psi) \mathcal{Q}_3, \quad B_{rl} = (\chi \tau + \frac{1}{2} \psi) \mathcal{Q}_1, \\ B_{rc} &= \varphi \tau + \frac{1}{2} (\mathbf{n} \cdot \mathbf{e}_k) + (\chi \tau + \frac{1}{2} \psi) \mathcal{Q}_2, \\ B_{rr} &= (\chi \tau + \frac{1}{2} \psi) \mathcal{Q}_3, \\ \mathcal{E}_{zl} &= \chi \mathcal{Q}_1, \quad \mathcal{E}_c = \varphi - \chi \mathcal{Q}_2, \quad \mathcal{E}_{zr} = \chi \mathcal{Q}_3. \end{aligned} \quad (43)$$

Eq. (42) is an equation for the pressure variable $p_{i+1,k}$ in a mirror cell outside the domain, see Fig. 3. The pressure at the new time level t^{n+1}

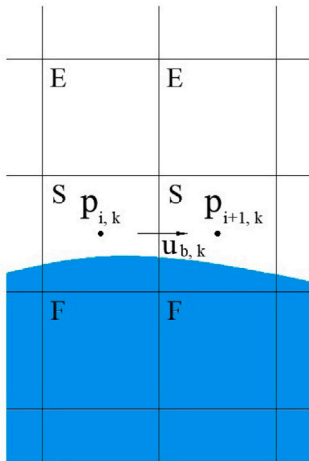


Fig. 4. No second derivatives of the solution variables are implemented at the free surface.

is located on the left-hand side, while on the right-hand side horizontal velocities including convective and diffusive terms at the old time level t^n are placed.

The stencil of the discrete ABC in (42) is similar to that of the pressure Poisson equation and can readily be combined with the equations for the inside of the domain. However, the matrix on the left-hand side includes the additional coefficients for the pressures $p_{i,k-1}$ and $p_{i,k+1}$ in Fig. 3 that are not part of the ‘normal’ five-point (in 2D) pressure Poisson stencil.

The second derivatives of the pressures and velocities in the vertical direction from three horizontal layers are required. No solution variables, however, are calculated above the free surface in one-phase flow simulations so that only information below the free surface is available, see Fig. 4.

The second derivatives of the velocities and pressures, which use only one-sided information, may result in unstable simulations. Therefore, in Surface cells (according to the labeling system in [23,24]), Sommerfeld condition (20), with a prescribed coefficient c_k , is implemented at the cost of accuracy.

Similarly, no solution variables are determined below the bottom of the computational domain, see Fig. 5. Therefore, constant extrapolation is applied to the velocity below the bottom, i.e. $u_{b,k-1} = u_{b,k}$. The dynamic part of the pressure below the bottom is also obtained from constant extrapolation, combined with a linear extrapolation of the hydrostatic part of the pressure, which results in $p_{b,k-1} = p_{b,k} + gz_{b,k-1}$.

7. Verification study

The (G)ABC with a mean flow in Eq. (42) is verified through comparison between reflection coefficients from simulation and theoretical reflection coefficients (Appendix). Regular and irregular waves in the presence of different flow velocities are taken into account. Both following mean flow, in the same direction as the waves, and opposing mean flow, in the opposite direction to the waves, are considered. All simulations are nonlinear. The simulations with regular waves and a higher value for kh are steeper than for lower kh . In simulations with steeper waves, the amplitudes of the higher-order wave components are larger. From the results we may interpret how that affects the performance of the boundary condition.

Regular wave simulations. The wave has a height of $H_w = 1.0$ m and the water depth h is 10 m for all simulations. Three following mean flows with magnitudes $U = 0.5, 1.0, 2.0$ m/s and two opposing flows $-0.5, -1.0$ m/s are accounted for. 25 values for kh of the monochromatic

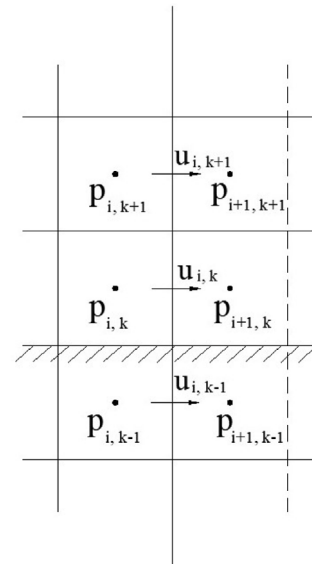


Fig. 5. The solution variables below the bottom are determined from the constant extrapolation of the solution variables above the bottom.

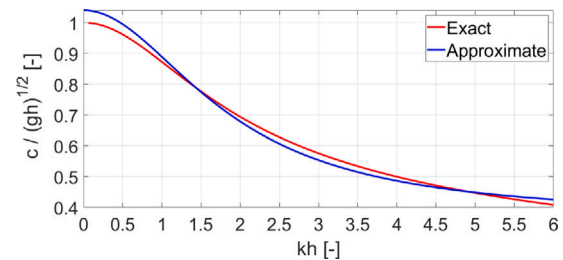


Fig. 6. Approximation of the dispersion relation.

waves vary from 0.2 to 5 evenly. The domain length L_d is selected to be one and a half wavelength L_w and thus 25 different domain sizes are used. The simulation duration is always 6 times of L_d / c_g , therefore, the duration is different for each simulation and the wave energy (group velocity c_g) travels 6 domain lengths in this duration.

The Sommerfeld condition with mean flow is perfect for one certain wave component and flow velocity. However, an irregular wave in reality is often composed of a number of components, each individual component has its own wave frequency, wave number and phase. Although a tuned Sommerfeld condition works better for regular waves, the (G)ABC is studied also with regular waves so that we may obtain a numerical reflection coefficient and compare it to the theoretical reflections to study its performance. To account for the dispersive properties of waves, the coefficients in the boundary condition GABC with flow can be chosen such that the dispersion relation and reflection coefficients of the waves with the kh in the range (0,6) are approximated well for irregular waves. With $a0 = 1.04$, $a1 = 0.106$, and $b1 = 0.289$, the approximate dispersion relation is illustrated in Fig. 6 and the theoretical reflection coefficient can be computed based on Appendix.

To obtain the numerical reflection coefficient, the outgoing and reflected waves should be distinguished at their respective wave numbers from the wave signals in the domain. The time history of the surface elevation at all grid points in the computational domain is adopted to perform Fourier analysis in both space and time. The 2D Fourier transform results in the wave amplitudes for a range of wave numbers. The wave numbers decomposed from the Fourier transform are located in the range $-2\pi[-N_x/2 : N_x/2 - 1]/(N_x \Delta x)$, in which N_x

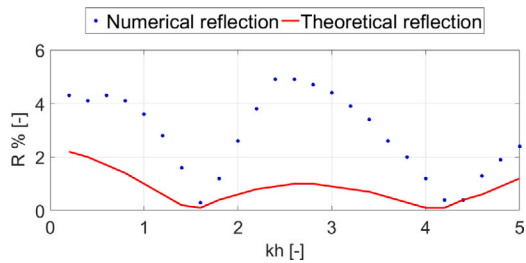


Fig. 7. Comparison between simulated and theoretical reflection coefficients for regular waves on following mean flow: $U = 0.5$ m/s.

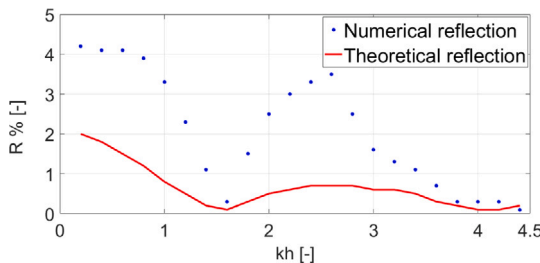


Fig. 8. Comparison between simulated and theoretical reflection coefficients for regular waves on following mean flow: $U = 1.0$ m/s.

is the number of grid cells in x -direction and Δx is the grid size. The number of time instances is denoted by N_t and the time step by Δt , respectively. Positive wave numbers correspond to the incoming wave components, negative wave numbers corresponds to the reflected wave components. The reflection coefficient is obtained from the ratio of the wave amplitudes of the positive wave number and the negative wave number associated with it through the dispersion relation. Therefore, no negative wave numbers are present in Figs. 7 through 11.

To measure the accuracy of the GABC with flow, the numerical reflection coefficients obtained from the above 125 test cases are compared with the theoretical ones, which are derived in the Appendix. Figs. 7 to 11, which correspond to the following magnitudes $U = 0.5, 1.0, 2.0$ m/s and the opposing flows $U = -0.5, -1.0$ m/s respectively, compare the numerical reflection coefficients obtained from the numerical simulations with the theoretical ones. All simulated reflection coefficients are lower than 5%, but larger than theoretical reflection coefficients. They are larger due to the fact that the second derivative of the solution variables could not be continued above the free surface and that an approximation needed to be made there. This was found from the working leading up to Wellens and Borsboom [23], for which the nonlinear implementation was compared to an implementation with linearized governing equations. In the implementation with linearized governing equations, the second derivative of the boundary condition near the free surface can be continued so that the performance in this situation could be compared to the situation with a Sommerfeld condition in the cell at the boundary near the free surface.

In Fig. 8, there are no reflected wave components for the kh values larger than 4.2, because they is no solution of the dispersion relation for those wave numbers. The reflection coefficients for the case $U = 2.0$ m/s in Fig. 9, have no reflected wave components for kh values larger than 1.4, because of the same reason.

The numerical reflection coefficients for regular waves on top of opposing flows are also compared with the theoretical values. The result for the flow magnitude $U = -0.5$ m/s is shown in Fig. 10. On the whole, the simulated reflections are larger than their theoretical counterparts, but for all the kh are less than 5 %. Given a stronger opposing mean flow $U = -1.0$ m/s, the simulated reflections show a similar tendency and are in good agreement with theory, see Fig. 11.

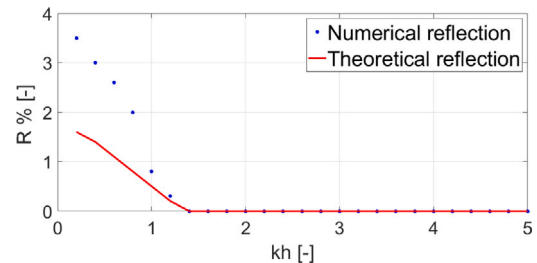


Fig. 9. Comparison between simulated and theoretical reflection coefficients for regular waves on following mean flow: $U = 2.0$ m/s. The reflections do not ever exist for kh values larger than 1.4.

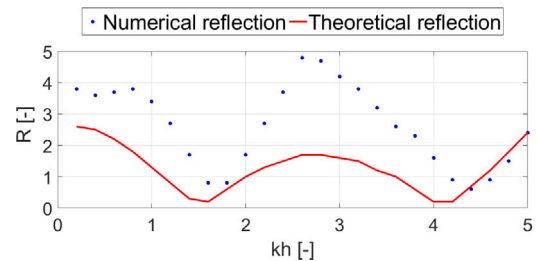


Fig. 10. Comparison between simulated and theoretical reflection coefficients for regular waves on following mean flow: $U = -0.5$ m/s.

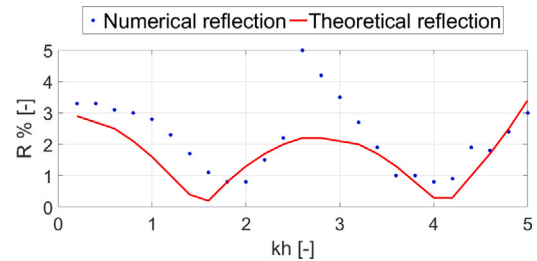


Fig. 11. Comparison between simulated and theoretical reflection coefficients for regular waves on following mean flow: $U = -1.0$ m/s.

The numerical reflection coefficients for the $kh \in [2.6, 3.0]$ are seemingly discontinuous. Because the simulation results themselves did not show anything out of the ordinary, the apparent discontinuity remains an ongoing investigation.

Irregular waves simulations. To further test the (G)ABC with mean flow, which has primarily been designed for simulations of long-crested irregular waves on top of a mean uniform flow, tests with irregular waves in combination with following and opposing flows have been performed in a 2D computational domain.

The performance of the boundary condition is measured by means of the reflection coefficients. A JONSWAP wave spectrum, see Table 1, on top of a mean flow, with GABC at both inflow and outflow end of the domain, is adopted to obtain the numerical reflection coefficients, which are compared with the theoretical counterparts.

Two simulations have been performed, in which the above JONSWAP spectrum is imposed on top of a following mean flow: 1.0 m/s and an opposing mean flow: -0.5 m/s, respectively. The domain has a length of 400 m. The finest grid size in both x and z -directions is 0.5 m. The duration of the simulations is specified as 1200 s for the accuracy of the Fourier transform. For the shortest incident wave period that has energy, 200 time steps per period are applied. For the smallest incident wavelength that has energy, 12 cells per wavelength are adopted. For those wave components the effect of numerical dispersion is not negligible. It is a compromise for reasons explained below.

Table 1
JONSWAP spectrum.

Parameter	Value
Peak period	6.0 [s]
Significant wave height	2.0 [m]

Table 2
Coefficients of ABC.

Parameter	Value
a0	1.04 [-]
a1	0.106 [-]
b1	0.289 [-]

The simulations start with a uniform mean flow, i.e. the flow magnitude is the same through the domain and no waves are present at $t = 0$. Waves are imposed at the inflow side of the domain using linear wave potential theory. The surface elevation and velocities at the inflow boundary are gradually built up by means of linear ramp function over an interval of two significant wave periods.

The coefficients of the GABC are the same as for the regular wave simulations, see Table 2. They are tuned in such a way that the reflection coefficients over the range of $kh \in (0, 6]$ are less than 2%. The coefficient in the Sommerfeld condition applied at the surface cells, which is the phase velocity of the outgoing wave, is tuned according to the peak component in the spectrum.

Here the procedure to extract the numerical reflection coefficients is different from what was used for regular waves, because the wave components going in different directions could not be identified so straightforwardly.

Note that for irregular waves there are some other widely-used methods to separate incident and reflected waves. For example, a 2-point method is proposed [36]. Here a simultaneous recordings of wave profiles is made at two adjacent locations on a line parallel to the direction of wave propagation. Since the 2-point method has limitations, a 3-point approach [37] was proposed, which uses a least square analysis for decomposing the measured spectra into incident and reflected spectra with greater accuracy and range.

Here, another method is adopted [23] that is more accurate for analyzing irregular waves than the methods referred for steeper sea states, but at the cost of more computational effort. First, a wave simulation is performed in a large domain of length 10,000 m, which is large enough that during the entire duration reflected waves cannot reach the measurement location. The required domain length is determined from the phase velocity of the fastest propagating wave components and the duration of the simulation: $L_d = \sqrt{gh}t_{max}$. Here h is the water depth.

In the meantime, another simulation is carried out in a small domain. This simulation is same as the previous one in the large domain in every aspect, except for the domain length and the boundary condition applied at the outflow end of the domain. Measurements of the surface elevation in the small domain, taken at exactly the same positions, are compared to measurements in the large domain. Their difference can only be attributed to the boundary condition since everything else is same. The large domain and small domain, with the measurement location in the middle of the small domain, are illustrated in Fig. 12. The simulation took 36 hours in the large domain and 25 minutes in the short domain to finish. The time required for the simulation in the large domain is the main reason why the compromise mentioned above was necessary, and why we did not adopt a small grid size.

Subtraction of the wave signal at the measurement location in the large domain from the wave signal in the small domain where the boundary condition GABC is applied results in a reflection signal. Subsequently, the wave signal in the large domain and the reflection signal are decomposed into their Fourier components, which are used to calculate the spectra and reflection coefficients. Note that this method disregards any nonlinearities such as wave-wave interactions. The

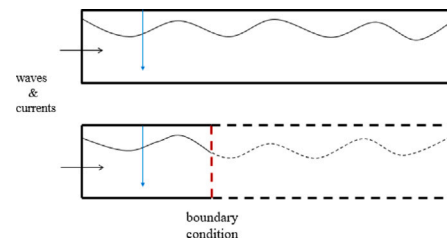


Fig. 12. Large and small domains used to obtain reflected signals in the middle of the small domain.

resulting input spectrum, reflected spectrum and reflection coefficients will be compared with theory, see Fig. 13.

First, the input spectrum obtained from the numerical simulation is given in Fig. 13(a), which shows reasonable agreement with the theoretical one. The reflected wave spectrum is shown in Fig. 13(b). A shift of the wave number of the reflected waves is visible due to the Doppler effect of the opposing mean flow on the reflected waves. The kh -axis is different from that in the other three figures, since the reflected modes have shorter wavelengths compared to the outgoing modes in the presence of the following mean flow. The NaN values indicate that reflected components do not exist for these wave frequencies (no solution of the dispersion relation).

The reflection coefficients in comparison with theory are illustrated in Fig. 13(c). The simulated reflections for the shorter waves are smaller than theory. This may be attributed to wave nonlinearity and insufficient grid resolution for these shorter waves. There is no more reflection for $kh > 4.24$, because the corresponding reflected wave modes have wave numbers for which a solution of the dispersion relation does not exist.

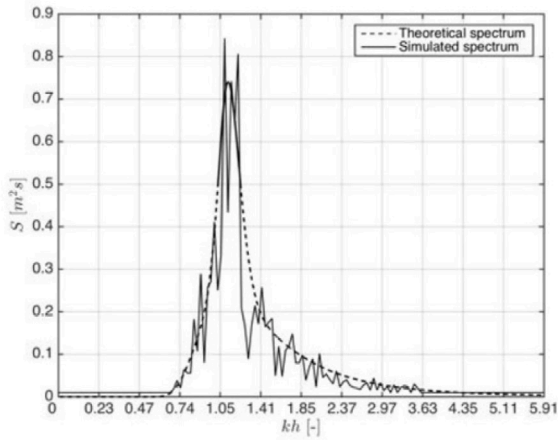
The procedure to post-process the results of irregular waves in an opposing mean flow is the same as what is used for a following mean flow. The flow velocity was equal to $U = -0.5$ m/s. Fig. 14 presents the input spectrum, reflected spectrum and reflection coefficients, which are numerically computed, in comparison with the theoretical reflection coefficient.

As can be observed in Fig. 14(a), the numerical input spectrum agrees well with the theoretical JONSWAP spectrum. Note that the kh -axis for the reflected spectrum (see Fig. 14(b)) is different from that in the previous figure, because the reflected wave modes have longer wavelengths than the corresponding outgoing modes in the presence of the opposing mean flow. For the other reflected wave components with $kh < 3.8$, which correspond with the outgoing modes with $kh < 6$, the reflected energy matches reasonably with theory. The difference is likely due to the steepness of the waves in the simulations. In Fig. 14(c), the reflection coefficients for different wave numbers are presented. For the wave modes with $3 < kh < 6$, the reflection coefficients are larger than the analytical results. This deviation is likely caused by the increased steepness in opposing flow, which adds to the nonlinear effects at the boundary.

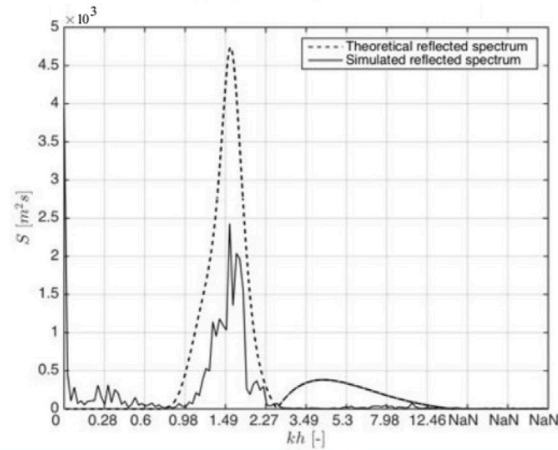
A final verification concerns the stability of the boundary condition with the coefficients that were chosen. For that a simulation with the same settings as the irregular wave simulations was performed, but for a duration that is ten times as long. The simulation was set to run until 10^4 s. Fig. 15 shows the free surface in the middle of the domain during that time. The free surface does not show exponential growth, which would be an indication of instability.

8. Validation study

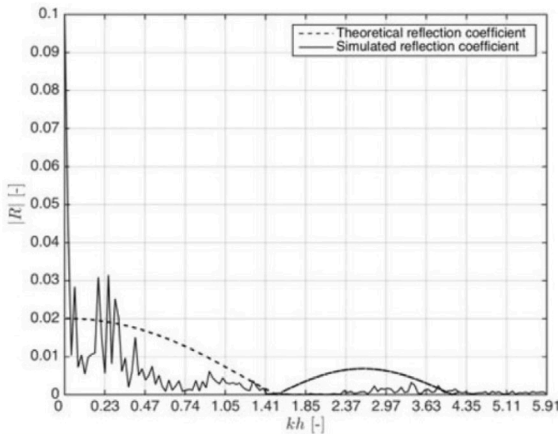
A validation study has been performed to demonstrate that the (G)ABC with flow can be applied in the real maritime applications. The simulated heave and pitch motions of a Wigley hull at forward speed in



(a) Input wave spectrum

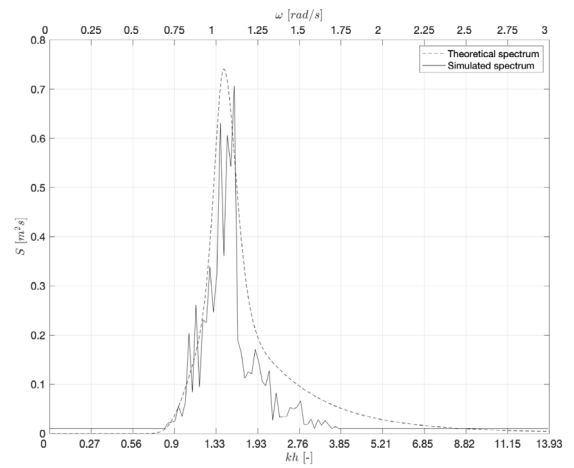


(b) Reflected wave spectrum

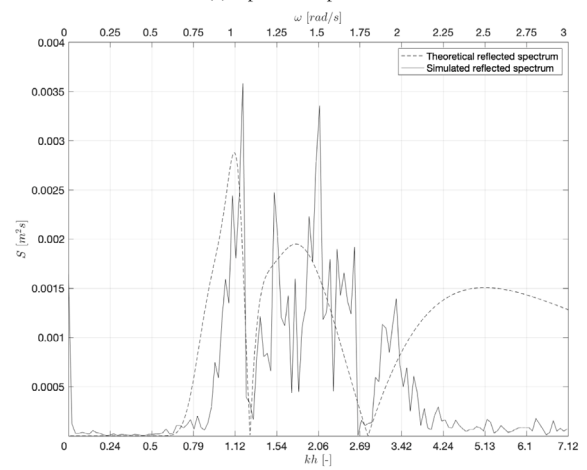


(c) Reflection coefficients

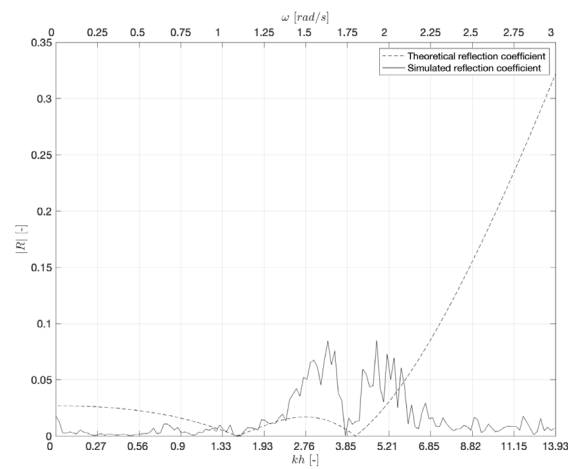
Fig. 13. Irregular wave simulation in comparison with theory: $U = 1.0$ m/s.



(a) Input wave spectrum



(b) Reflected wave spectrum



(c) Reflection coefficients

Fig. 14. Irregular wave simulation in comparison with theory: $U = -0.5$ m/s.

both regular and irregular waves are compared with the experimental results.

The experimental tests of a Wigley hull have been specifically designed for validation and carried out in the towing tank of Delft University of Technology, see Fig. 16. The data of the experiment are shared as open data [38]. The hull is based on the Wigley parameter for the length $L = 3$ m, the width $B = 0.3$ m and the draft $T = 0.1875$ m. However, the actual draft of the model in the experiment is 0.2 m, which

is different from the T in the Wigley parameter set. The ship parameters used in the experiments and simulations are presented in Table 3.

The motions of the Wigley hull are measured through two vertical position gauges, located half a meter away from the center of gravity (CoG) of the model. Then the heave and pitch motions at the CoG of the

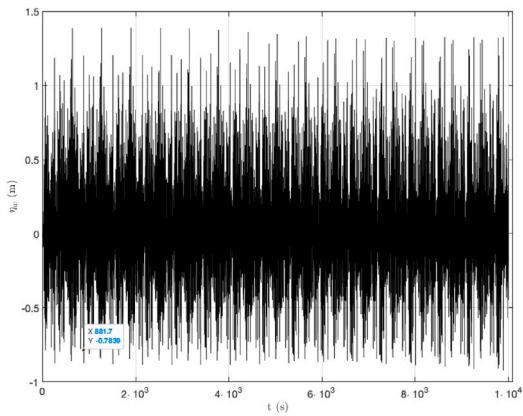


Fig. 15. Stability demonstration: long duration simulation showing free surface in the middle of the computational domain.



Fig. 16. The wigley hull model in the towing tank.

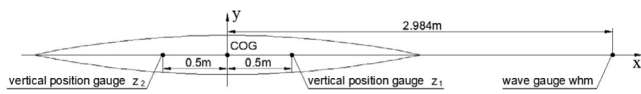


Fig. 17. Vertical position gauges on the ship model.

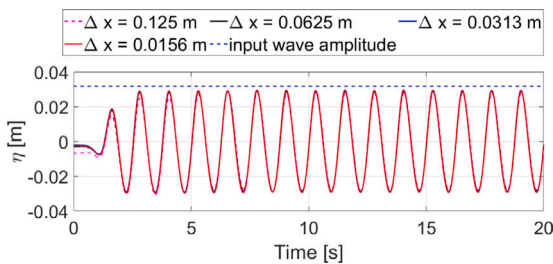


Fig. 18. Time history of surface elevations for four grid resolutions.

Table 3
Ship parameters used in the experiments and simulations. J22 is the radius of inertia for pitch.

L (m)	B (m)	T (m)	Mass (Kg)	J22 (m)
3.0	0.3	0.2	81.9	0.64

hull can be calculated. Fig. 17 shows the positions of the measurement instruments which will be utilized to compare the simulated results with the experimental results. The wave gauge *whm*, which is fixed to the carriage and located at a distance of 2.984 m away from the center of gravity (CoG), measures the surface elevations. The measurements stop as soon as reflected waves from the beach start to arrive at the model in the tank. Several sea states such as regular and irregular long-crested waves, and different forward speeds are imposed on the Wigley hull.

Table 4
Wave heights, periods, lengths and ship forward speeds in the regular wave experiments.

Run ID	H [m]	T [s]	U [m/s]
77	0.057	1.25	1.0
79	0.052	1.645	0.5

Grid study. The aim of the grid study is to obtain sufficient grid resolution for representing the input, according to the measurements in the experiments without the Wigley model present. The grid study simulations are performed in 2D computational domains. The domain size in *x*-direction was chosen to correspond to five wave lengths. The water depth is specified as 0.73 m in line with the depth in the experiment.

At $t = 0$ the wave is generated with velocities according to Airy theory and ramped up linearly over two wave periods to the full amplitude into the computational domain. At every time step after the initial condition, the flow variables at the boundary are calculated according to the Airy wave theory, and prescribed at the inflow boundary.

Four simulations are performed to investigate which grid resolution suffices. The input wave height is 0.0633 m, and the period is 1.25 m. The first simulation is performed with a mesh size of $\Delta x = 0.125$ m on a uniform grid. With the same wave, the mesh sizes for the other three tests are refined to $\Delta x = 0.0625$, 0.0313 and 0.0156 m, respectively.

At both inflow and outflow boundary, the first-order generating and absorbing boundary condition (GABC) with a mean flow is applied. A free-slip condition is employed at the remaining sides of the computational domain, as it allows for a coarser grid near those boundaries.

The simulated surface elevations measured slightly inside the domain are depicted in Fig. 18. With the grid refined by a factor of 2 in three successive tests, the simulated wave amplitudes increase from 0.0282 m to 0.0289 m, 0.0291 m and finally 0.0294 m. As can be seen, it is 7% smaller than the expected wave amplitude 0.0316 m, which is acceptable for engineering application. A difference between the experiment and the simulation remains, because linear wave theory is adopted to generate waves, while the method is nonlinear. This creates a mismatch at the inflow boundary that does not go away when the simulation results converge.

With a refinement factor of 2, the computational cost increases by a factor of 2^4 . Considering the number of grid cells and the simulation durations adopted in the later simulations in this work, further refinement level will make the simulations too expensive. In order to obtain the desired wave height, our strategy is to specify a slightly higher input wave height in the simulation with the finest grid in our test, with $\Delta x = 0.0156$ m, that is still affordable in terms of computational cost.

Wigley model advancing in regular waves. First, two simulations of the Wigley model in regular waves are chosen to investigate how the ship motions change when the domain boundary is located closer to the structure. Two waves are chosen from two tests 77 and 79 in the experiments, in which different forward speeds of the ship are considered. The test identification numbers of the experiments with regular waves are given in Table 4, with the wave heights, periods, lengths and ship forward speeds associated with these tests.

In simulation 77, the Wigley model is positioned a distance of two ship lengths away from the inflow boundary. Another two ship lengths are left on the downstream side of the hull. Consequently, the size of the domain in *x*-direction becomes $L_x = 5L = 15$ m. In *y*-direction, the width of the domain is selected the same as that in the experiment, which is $L_y = 2.75$ m. The water depth is specified as 0.73 m, the same as in the experimental towing tank.

For simulation 79, the dimension of the computational domain in the *x*-direction is $L_x = 3.33L = 10$ m, which is smaller than the domain

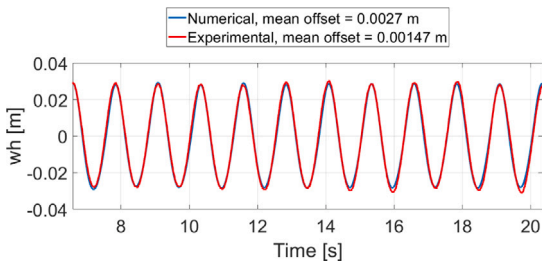


Fig. 19. The comparison of numerical and experimental surface elevation for test 77.

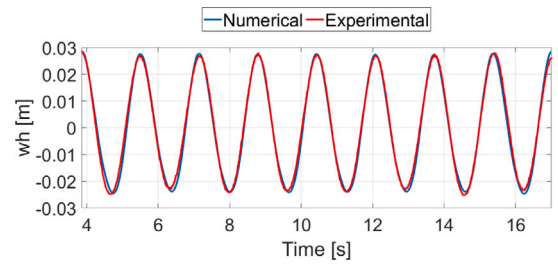


Fig. 21. The comparison of numerical and experimental surface elevation for the test 79.

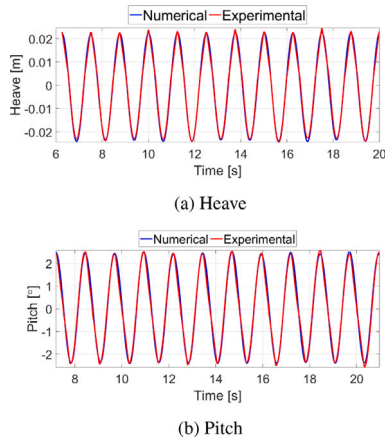


Fig. 20. Numerical results of the heave and pitch motion for the test 77.

size $L = 15$ m in the test 77. The width and water depth are taken as 2.75 m and 0.73 m, which are identical to those in the test 77.

The mesh for these two simulations is kept constant at $\Delta x = \Delta y = \Delta z = 0.0156$ m in all three directions. The GABC with mean flow is applied at both inflow and outflow boundaries. For test 77, first the water surface elevation measured at 2.984 m in front of the Wigley model is presented in Fig. 19. It can be seen that the resulting wave height from the numerical simulation is 0.057 m, which is identical as measured in the experiment. With this wave, the results of heave and pitch motions are obtained, see Figs. 20(a) and 20(b). The simulated heave amplitude has a value of 0.023 m, which is the same as in the experiment. The pitch amplitudes measured in both the simulation and experiment are 2.45°.

For the test 79, the domain size is 2/3 of that in the test 77. The surface elevation measured at 2.984 m in front of the ship model is shown in Fig. 21. The wave heights for both the simulation and experiment are 0.052 m. The resulting heave and pitch motions for the test 79 in the simulation and experiment are shown in Figs. 22(a) and 22(b), respectively. The average heave amplitude of 0.018 m is obtained in the simulation, which agrees with that in the experiment. The simulated and experimental pitch amplitudes are both 1.57°.

It can be concluded from these results that the boundary condition GABC with mean flow works as well in the smaller domain of test 79 as in the large domain of test 77, for the Wigley hull at forward speed in regular waves with the same grid size. The domain boundaries can be located quite near to the model using this boundary condition.

Wigley model advancing in irregular waves. In test 63, the Wigley model encounters an irregular wave, with significant wave height 0.006 m and peak period 1.39 s, causing wave diffraction and ship motions. The forward speed of the hull in this test is 0.5 m/s, and thus the Froude number is $Fr = 0.092$.

To obtain the input wave signals for the numerical simulation, the wave signal from $t = 42$ s to $t = 102$ s, measured by the wave gauge

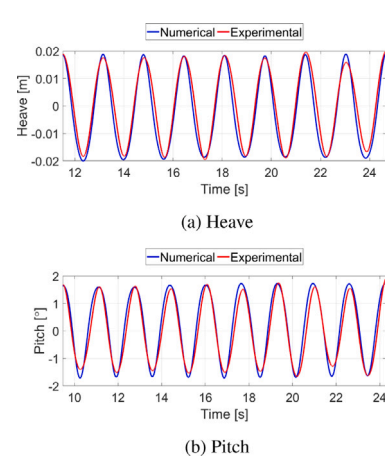


Fig. 22. Numerical results of the heave and pitch motion for the test 79.

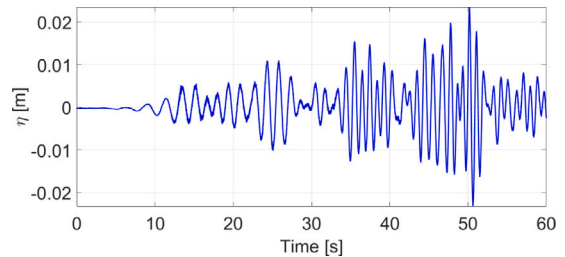


Fig. 23. Time history of the wave from $t = 42$ s to $t = 102$ s in the experiment 63.

located at 2.984 m away from the center of gravity of the Wigley model, is taken. That part of the signal contains within itself the transition between sailing in calm water to when the model first encounters the waves that are generated. The signal is shown in Fig. 23.

By means of a Fourier transform of the wave signal, the individual wave components with encounter frequencies are obtained. These frequencies need to be transformed to earth-fixed values as input in the numerical simulation. The extent of the computational domain in the horizontal direction is 12 m. The width of the domain is 2.75 m which is the same as in the experiment. The water depth has a value of 0.73 m, also the same as in the experiment. The boundary condition GABC with mean flow is applied at the outflow boundary of the domain. The grid size in all three directions is $\Delta x = \Delta y = \Delta z = 0.0156$ m, which results in 10 million grid points. The time step varies according to the Courant criterion, but is never larger than 0.025 s.

First the time series of simulated surface elevation at the inflow boundary is compared with the experimental results. For visualization, the experimental surface elevation is shifted in time from $t = 42$ s to $t = 0$, as shown in Fig. 24. In the first 10 seconds, the simulated elevation oscillates around the mean level, which is an artifact of not sending in the shortest wave components from the Fourier transform,

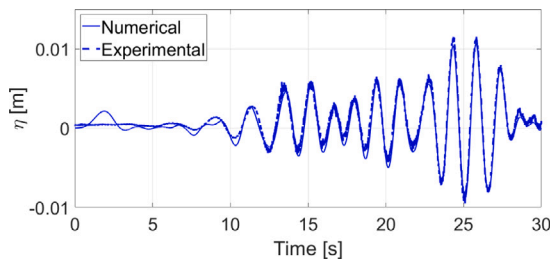


Fig. 24. Surface elevation for test 63.

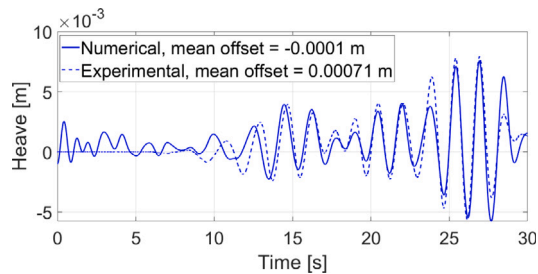


Fig. 25. Heave motion for test 63.

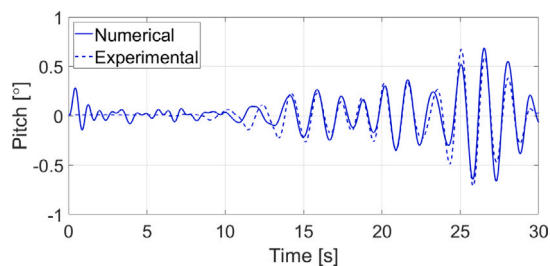


Fig. 26. Pitch motion for test 63.

because they have the tendency to cause high velocities near the free surface. From $t = 10$ s until the end of the simulation, the root mean square error between the simulated and experimental surface elevation is 0.001 m, which is acceptable.

With the input wave, the resulting heave and pitch motions of the Wigley model in the simulation are obtained and compared with the experimental data in Figs. 25 and 26, respectively. There is a mean offset in both simulated and experimental heave motions, which is removed in the figure for comparison. There is a phase lag between two curves in the time interval between 10 and 15 seconds. After that the phase difference disappears. The simulated heave signal is lower than the experimental data between $t = 17$ s and $t = 25$ s and higher for the rest of the time. The root mean square error between the simulation and experiment is 0.0011 m, also acceptable. Comparing the pitch motion, a slight phase difference between simulated and experimental results is also present but smaller than in the heave motion. The root mean square difference between the pitch signal obtained from the simulation and the signal from the experiment is 0.09° .

The simulation of a Wigley model at forward speed in irregular head waves has good agreement with the experiment. This indicates that the GABC with a mean flow not only works well for theoretical conditions with only regular or irregular waves, but also for cases where the ship generated waves are present. A significant difference between the theoretical simulations and the simulations of the ship model is the wave system that is stationary with respect to the ship. The stationary wave system leads to a change of the mean free surface around the ship. The comparison between the simulation and the experiment therefore

also demonstrates that the ship generated stationary waves do not disturb the GABC's performance.

9. Conclusions

This paper discusses the background, derivation, implementation and results of a generating absorbing boundary condition (GABC) for waves in the presence of a mean uniform flow. The GABC is obtained from the decomposition of the planar equation including flow. Being based on potential flow theory, use of the boundary condition is limited to locations where waves are not expected to break, e.g. very close to the structure and in the surf zone in coastal modeling. Combining the boundary condition with an approximation of the dispersion relation and vertical derivatives of the solution variables near the boundary, yields a condition with little reflection for a range of wave numbers. This is advantageous for irregular wave simulations. The range of dimensionless wave numbers investigated here was between 0 and 6. The fact that linearized potential theory was used locally at the boundary instead of nonlinear potential theory was argued not to limit the performance of the boundary condition considerably.

In simulations of regular and irregular waves on top of a mean flow, the ABC with flow performs as well as in experimental facilities for waves, with the reflection coefficients as low as 5% for mildly steep waves over a range of frequencies. Various flow velocities up to 2 m/s and different directions, both following and opposing, have been taken into account. The main discrepancies between numerical and theoretical reflections for steeper waves are caused by the implementation of the Sommerfeld condition near the free surface of the boundary condition. Other discrepancies, to a limited extent, can be attributed to the fact that linear theory is used to generate these waves and to derive the boundary condition, which may cause a small mismatch. The latter, in particular, shows for cases with opposing flow, in which the steepness was significant as a result of the shorter wave lengths in these conditions.

The validation study indicates that GABC not only works well for theoretical conditions with waves only, but also for cases where ship generated waves are present. The comparison between the simulations and the experiment demonstrates ship interaction with waves is captured well by the numerical method with the GABC at the boundaries.

CRediT authorship contribution statement

X. Chang: Formal analysis, Investigation, Methodology, Software, Writing – original draft. **P.R. Wellens:** Conceptualization, Data curation, Formal analysis, Funding acquisition, Investigation, Methodology, Project administration, Resources, Software, Supervision, Validation, Visualization, Writing – original draft, Writing – review & editing.

Declaration of competing interest

The authors declare that they have no known competing financial interests or personal relationships that could have appeared to influence the work reported in this paper.

Data availability

The data will be made open access, if the article were to be published.

Acknowledgment

This research is financially supported by the program of China Scholarship Council (CSC) with project NO. 201406950033.

Appendix

In this appendix, the theoretical reflection coefficient for the Sommerfeld condition incorporating uniform mean flow in a 1D domain is derived.

Consider the Sommerfeld condition applied to a wave potential function ϕ_w and constant mean flow U :

$$[\partial/\partial t + (c_{bc} + U)\partial/\partial x]\phi_w = 0, \quad (44)$$

in which c_{bc} is a tuning parameter, which is an approximation of the intrinsic celerity, i.e. without flow. The condition (44) is formulated in x -direction.

Suppose that an outgoing wave component and its reflected component can be identified. Then, the wave potential function ϕ_w can be written as a combination of the outgoing wave potential and reflected wave potential:

$$\begin{aligned} \phi &= \phi_{out} + \phi_{refl}, \\ \phi_{out} &= A_{out} e^{i(\omega t - k_{out} x + \theta_{out})}, \quad \phi_{refl} = A_{refl} e^{i(\omega t - k_{refl} x + \theta_{refl})} \end{aligned} \quad (45)$$

where A_{out} and A_{refl} are the amplitudes of the respective wave modes. k_{out} and k_{refl} are the wave numbers of the outgoing wave and reflected wave mode, respectively.

Note that the outgoing wave mode propagates along the positive x -direction. The reflected wave mode is produced by the outgoing wave mode when the Sommerfeld condition is not perfectly tuned to the wave mode. Accordingly, this reflected wave mode propagates in the opposite direction of the outgoing wave mode, i.e. along the negative x -direction. Hence, the wave number k_{refl} is negative.

Since we have the relation $\omega t_0 - k_{out} x_{bc} + \theta_{out} = \omega t_0 - k_{refl} x_{bc} + \theta_{refl}$ at a certain time $t = t_0$ at the boundary $x = x_{bc}$, the phase for the reflected mode θ_{refl} can be expressed as:

$$\theta_{refl} = \theta_{out} + (k_{refl} - k_{out})x_{bc}. \quad (46)$$

The wave numbers k_{out} and k_{refl} are obtained from the dispersion relation as follows:

$$\omega - kU = \pm \sqrt{gk \tanh(kh)} \quad (47)$$

To obtain the reflection coefficient, the following derivatives are required:

$$\begin{aligned} \partial\phi_{out}/\partial t &= i\omega\phi_{out}, \quad \partial\phi_{refl}/\partial t = i\omega\phi_{refl} \\ \partial\phi_{out}/\partial x &= -ik_{out}\phi_{out}, \quad \partial\phi_{refl}/\partial x = -ik_{refl}\phi_{refl}. \end{aligned} \quad (48)$$

Substitution of the relations in (48) into Eq. (44) and evaluation of the obtained expression yields:

$$\begin{aligned} [\omega - (c_{bc} + U)k_{out}]A_{out} e^{i(\omega t - k_{out} x + \theta_{out})} \\ + [\omega - (c_{bc} + U)k_{refl}]A_{refl} e^{i(\omega t - k_{refl} x + \theta_{refl})} = 0. \end{aligned} \quad (49)$$

Then the reflection coefficient at the boundary $x = x_{bc}$ is determined as:

$$R = \frac{A_{refl}}{A_{out}} = - \frac{[(c_{bc} + U)k_{out} - \omega] e^{i(\omega t - k_{out} x_{bc} + \theta_{out})}}{[(c_{bc} + U)k_{refl} - \omega] e^{i(\omega t - k_{refl} x_{bc} + \theta_{refl})}}. \quad (50)$$

Since the relation (46) at the boundary $x = x_{bc}$ holds, the reflection coefficient R can be further written as:

$$\begin{aligned} R &= - \frac{(c_{bc} + U)k_{out} - \omega}{(c_{bc} + U)k_{refl} - \omega} \\ &= - \frac{k_{out}/\omega - 1/(c_{bc} + U)}{k_{refl}/\omega - 1/(c_{bc} + U)}. \end{aligned} \quad (51)$$

References

- [1] Peric R, Abdel-Maksoud M. Reliable damping of free surface waves in numerical simulations. *Ship Technol Res* 2016;63.
- [2] Carmigniani RA, Violeau D. Optimal sponge layer for water waves numerical models. *Ocean Eng* 2018;163:169–82.
- [3] Choi YM, Kim YJ, Bouscasse B, Seng S, Gentaz L, Ferrant P. Performance of different techniques of generation and absorption of free surface waves in computational fluid dynamics. *Ocean Eng* 2020;214:107575.
- [4] Wang D, Dong S. A discussion of numerical wave absorption using sponge layer methods. *Ocean Eng* 2022;247:110732.
- [5] Zhang C, Lin N, Tang Y, Zhao C. A sharp interface immersed boundary/VOF model coupled with wave generating and absorbing options for wave-structure interaction. *Comput & Fluids* 2014;89:214–31.
- [6] Colombo A, Crivellini A. Assessment of a sponge layer non-reflecting boundary treatment for high-order CAA/CFD computations. *Comput & Fluids* 2016;140:478–99.
- [7] Vukcevic V, Jasak H, Malenica S. Decomposition model for naval hydrodynamic applications. Part I: Computational method. *Ocean Eng* 2016a;121:37–46.
- [8] Vukcevic V, Jasak H, Malenica S. Decomposition model for naval hydrodynamic applications. Part II: Verification and validation. *Ocean Eng* 2016b;121:76–88.
- [9] Altomare C, Tagliafierro B, Dominguez J, Suzuki T, Viccione G. Improved relaxation zone method in SPH-based model for coastal engineering applications. *Appl Ocean Res* 2018;81:15–33.
- [10] Peric R, Abdel-Maksoud M. Analytical prediction of reflection coefficients for wave absorbing layers in flow simulations of regular free surface waves. *Ocean Eng* 2018;147:132–47.
- [11] Peric R, Vukcevic V, Abdel-Maksoud M, Jasak H. Optimizing wave generation and wave damping in 3D-flow simulations with implicit relaxation zones. *Ocean Eng* 2018;147:132–47.
- [12] Santo H, Taylor PH, Bai W, Choo YS. Current blockage in a numerical wave tank: 3D simulations of regular waves and current through a porous tower. *Comput & Fluids* 2015;115:256–69.
- [13] Christou A, Stoesser T, Xie Z. A large-eddy-simulation-based numerical wave tank for three-dimensional wave-structure interaction. *Comput & Fluids* 2021;231:105179.
- [14] Higuera P. Enhancing active wave absorption in RANS models. *Appl Ocean Res* 2020;94:102000.
- [15] Higuera P, Lara J, Losada I. Realistic wave generation and active wave absorption for Navier-Stokes models. *Coast Eng* 2013;71:102–18.
- [16] Higuera P, Losada I, Lara J. Three dimensional numerical wave generation with moving boundaries. *Coast Eng* 2015;101:35–47.
- [17] Tsynkov SV. Numerical solutions of problems on unbounded domains. A review. *Appl Numer Math* 1998;27(4):465–532.
- [18] Wellens PR. Wave simulation in truncated domains for offshore applications (Ph.D. thesis, Delft University of Technology; 2012).
- [19] Brocchini M, Dodd N. Nonlinear shallow water equation modeling for coastal engineering. *J Waterw, Port, Coast Ocean Eng* 2008;134(2):104–20.
- [20] Hagstrom T, Warburton T. Complete radiation boundary conditions: minimizing the long time error growth of local methods. *SIAM J Numer Anal* 2009;47:3678–704.
- [21] Hagstrom T, Bécache E, Givoli D, Stein K. Complete radiation boundary conditions for convective waves. *Commun Comput Phys* 2012;11:610–28.
- [22] Duz B, Borsboom MJA, Veldman AEP, Wellens PR, Huijsmans RHM. An absorbing boundary condition for free surface water waves. *Comput & Fluids* 2017;156:562–78.
- [23] Wellens PR, Borsboom MJA. A generating and absorbing boundary condition for dispersive waves in detailed simulations of free-surface flow interaction with marine structures. *Comput & Fluids* 2020;200:104387.
- [24] Kleefsman K, Fekken G, A. V, Iwanowski B, Buchner B. A volume-of-fluid based simulation method for wave impact problems. *J Comput Phys* 2005;206:363–93.
- [25] Engquist B, Majda A. Absorbing boundary conditions for numerical simulation of waves. *Math Comp* 1977;74(5):1765–6.
- [26] Higdon RL. Absorbing boundary conditions for difference approximations to the multi-dimensional wave equation. *Math Comp* 1986;47(176):437–59.
- [27] Orlanski I. A simple boundary condition for unbounded hyperbolic flows. *J Comput Phys* 1976;21(3):251–69.
- [28] Blayo E, Debreu L. Revisiting open boundary conditions from the point of view of characteristic variables. *Ocean Model* 2005;9:231–52.
- [29] Verboom GK, Slob A. Weakly-reflective boundary conditions for two dimensional shallow water flow problems. *Adv Water Resour* 1984;7(4):192–7.
- [30] Van Dongeren A, Svendsen I. Absorbing-generating boundary condition for shallow water models. *J Waterw, Port, Coast Ocean Eng* 1997;123(6):303–13.
- [31] Lindman EL. Free space boundary conditions for the time dependent wave equations. *J Comput Phys* 1975;18:66–78.
- [32] Clayton RW, Engquist B. Absorbing boundary conditions for wave-equation migration. *Geophysics* 1980;45(5):895–904.
- [33] Keys RG. Absorbing boundary conditions for acoustic media. *Geophysics* 1985;50(6):892–902.

- [34] Peregrine DH. Interaction of water waves and currents. *Adv Appl Mech* 1976;16:9–117.
- [35] Peregrine DH, Jonsson IG. Interaction of waves and currents. U S Army Coast Eng Res Cent 1983.
- [36] Goda Y, Suzuki Y. Estimation of incident and reflected waves in random wave experiments. In: *Proceedings of the 15th International Conference on Coastal Engineering*, vol. 1, (15):1976, p. 828–45.
- [37] Mansard E, Funke E. The measurement of incident and reflected spectra using a least squares method. In: *Proceedings of the 17th International Conference on Coastal Engineering*, vol. 1, (17):1980, p. 154–72.
- [38] Wellens P. Experimental data for a wigley hull at forward speed in regular and irregular waves. 2020, <http://dx.doi.org/10.4121/21320604>, 4TU.ResearchData.